

## Automated detection, 3D segmentation and analysis of high resolution spine MR images using statistical shape models

This content has been downloaded from IOPscience. Please scroll down to see the full text.

2012 Phys. Med. Biol. 57 8357

(<http://iopscience.iop.org/0031-9155/57/24/8357>)

View [the table of contents for this issue](#), or go to the [journal homepage](#) for more

Download details:

IP Address: 129.89.130.68

This content was downloaded on 28/03/2017 at 00:26

Please note that [terms and conditions apply](#).

You may also be interested in:

[3D segmentation of annulus fibrosus and nucleus pulposus from T2-weighted magnetic resonance images](#)

Isaac Castro-Mateos, Jose M Pozo, Peter E Eltes et al.

[Automated bone segmentation from large field of view 3D MR images of the hip joint](#)

Ying Xia, Jurgen Fripp, Shekhar S Chandra et al.

[Automatic bone segmentation and bone-cartilage interface extraction for the shoulder joint from magnetic resonance images](#)

Zhengyi Yang, Jurgen Fripp, Shekhar S Chandra et al.

[Automatic hip cartilage segmentation from 3D MR images using arc-weighted graph searching](#)

Ying Xia, Shekhar S Chandra, Craig Engstrom et al.

[Registration of MRI to intraoperative radiographs for target localization in spinal interventions](#)

T De Silva, A Uneri, M D Ketcha et al.

[Automated detection of spinal centrelines, vertebral bodies and intervertebral discs](#)

Darko Štern, Boštjan Likar, Franjo Pernuš et al.

[Automatic extraction of the bone--cartilage interface from MRIs of the knee](#)

Jurgen Fripp, Stuart Crozier, Simon K Warfield et al.

[Parametric modelling and segmentation of vertebral bodies in 3D CT and MR spine images](#)

Darko Štern, Boštjan Likar, Franjo Pernuš et al.

[A combinatorial Bayesian and Dirichlet model for prostate MR image segmentation using probabilistic image features](#)

Ang Li, Changyang Li, Xiuying Wang et al.

# Automated detection, 3D segmentation and analysis of high resolution spine MR images using statistical shape models

A Neubert<sup>1,2</sup>, J Fripp<sup>1</sup>, C Engstrom<sup>3</sup>, R Schwarz<sup>4</sup>, L Lauer<sup>4</sup>,  
O Salvado<sup>1</sup> and S Crozier<sup>2</sup>

<sup>1</sup> The Australian E-Health Research Centre, CSIRO ICT Centre, Brisbane, Australia

<sup>2</sup> School of Information Technology and Electrical Engineering, University of Queensland, Brisbane, Australia

<sup>3</sup> School of Human Movement Studies, University of Queensland, Brisbane, Australia

<sup>4</sup> Siemens Healthcare, Erlangen, Germany

E-mail: [ales.neubert@uqconnect.edu.au](mailto:ales.neubert@uqconnect.edu.au)

Received 17 July 2012, in final form 25 October 2012

Published 30 November 2012

Online at [stacks.iop.org/PMB/57/8357](http://stacks.iop.org/PMB/57/8357)

## Abstract

Recent advances in high resolution magnetic resonance (MR) imaging of the spine provide a basis for the automated assessment of intervertebral disc (IVD) and vertebral body (VB) anatomy. High resolution three-dimensional (3D) morphological information contained in these images may be useful for early detection and monitoring of common spine disorders, such as disc degeneration. This work proposes an automated approach to extract the 3D segmentations of lumbar and thoracic IVDs and VBs from MR images using statistical shape analysis and registration of grey level intensity profiles. The algorithm was validated on a dataset of volumetric scans of the thoracolumbar spine of asymptomatic volunteers obtained on a 3T scanner using the relatively new 3D T2-weighted SPACE pulse sequence. Manual segmentations and expert radiological findings of early signs of disc degeneration were used in the validation. There was good agreement between manual and automated segmentation of the IVD and VB volumes with the mean Dice scores of  $0.89 \pm 0.04$  and  $0.91 \pm 0.02$  and mean absolute surface distances of  $0.55 \pm 0.18$  mm and  $0.67 \pm 0.17$  mm respectively. The method compares favourably to existing 3D MR segmentation techniques for VBs. This is the first time IVDs have been automatically segmented from 3D volumetric scans and shape parameters obtained were used in preliminary analyses to accurately classify (100% sensitivity, 98.3% specificity) disc abnormalities associated with early degenerative changes.

(Some figures may appear in colour only in the online journal)

## 1. Introduction

Disorders of the human vertebral column account for a significant proportion of musculoskeletal complaints (Woolf and Pfleger 2003). Magnetic resonance (MR) and computed tomography (CT) imaging have become key investigative tools in clinical decision making for pathological conditions of the vertebral column (Fries *et al* 2008, Cousins and Haughton 2009). Given its excellent soft tissue contrast, MR has emerged as the modality of choice for imaging intervertebral disc (IVD) related abnormalities, such as disc degeneration (Emch and Modic 2011). Given the high prevalence of degenerative disc disease findings on MR images in the asymptomatic population (Emch and Modic 2011), the clinical assessment of these early degenerative changes is an area requiring further investigation (Auerbach *et al* 2006). Indeed, the precise role of MR imaging in providing predictive and prognostic information on IVD degenerative processes is still unclear (Emch and Modic 2011). Current MR investigations into the multifactorial pathogenesis of disc degeneration seek to combine tissue signal and structural characteristics of IVDs (Yu *et al* 2011). Since most current clinical MR studies are acquired in two dimensions (2D), with relatively large inter-slice gaps compared to the in-plane resolution, only elementary 2D measures (e.g. disc height, height to width ratio) have been reported in the literature to quantify morphological changes of the IVDs (Berger *et al* 2011).

Recently, a number of 3D MR pulse sequences such as SPACE (Sampling Perfection with Application optimized Contrasts using different flip angle Evolution) have been developed (Lichy *et al* 2005) that generate 3D images of the spine at spatial resolutions comparable to CT, but without the associated ionizing radiation. These 3D MR sequences provide high resolution images of the IVDs and vertebral bodies (VBs) well suited for highly detailed morphometric studies on multi-dimensional size and shape parameters (e.g. volume, height/thickness, wedging/distortion) of these spinal column elements (figure 1). These quantities are of particular interest as surrogate measures for identifying discs with signs of early degeneration and for monitoring of longitudinal changes. However, the time cost involved with quantification of the 3D morphological information from volumetric images makes any manual segmentation procedures impractical.

In this paper, we present an automated 3D segmentation algorithm for detection, segmentation and morphological assessment of IVDs and VBs from high resolution 3D MR images of the thoracolumbar spine for potential clinical applications concerned with early detection and quantification of anatomical features. The development of an accurate automated segmentation method, as opposed to time- and expertise-intensive manual segmentation approaches, offers significant opportunities for both routine clinical implementation and large-scale trials, providing a standardized baseline for morphological assessment. Technical challenges arise from factors such as the inherent anatomical complexity and length of the vertebral column, intra- and inter-subject variations within and across the local spinal regions and several underlying MR imaging artefacts. The approach in this paper compares successfully to results available in the literature while, to the best of our knowledge, it is the first time intervertebral discs have been automatically segmented intrinsically in 3D from volumetric MR scans. Shape parameters obtained were used in preliminary analyses to accurately classify disc abnormalities associated with early degenerative changes, suggesting the higher order 3D morphologic information extracted from IVDs can encode relevant anatomical information.

### 1.1. Previous work

Previous segmentations of the bony vertebrae have used CT images while soft tissue segmentation approaches (including IVDs) have used MR. The high bone contrast in CT

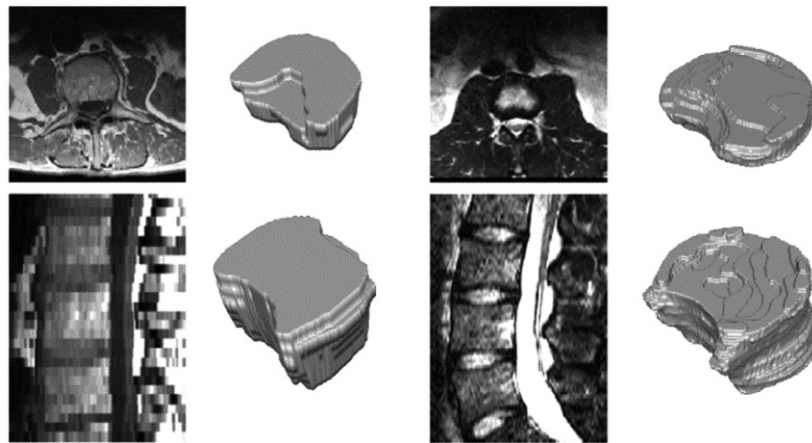


**Figure 1.** Example T1w 2D (left, 4 mm thick slices) and T2w 3D (right, 1 mm slices) MR scans and manual segmentations of an IVD (top) and a VB (bottom). The high resolution 3D image provides information about the anatomical shape that is not available in the 2D scan.

enables segmentation of the VBs using edge detection or region growing techniques (Kim and Kim 2009). The generalized Hough transform (Ballard 1981) was used together with 3D statistical models of shapes, gradient and appearance by Klinder *et al* (2009) achieving competitive results both in vertebrae identification and segmentation. Further improvements in speed and accuracy was achieved by using a trained 3D bone-structure edge detector together with a deformable statistical shape model (SSM) by Ma *et al* (2010). In general, the sharp intensity edges at bone boundaries are key determinants for accurate vertebrae localization and segmentation in CT. A popular way to incorporate the prior knowledge of the complex vertebrae shapes is via SSMs.

Segmentation of the VBs from MR images is often based on 2D object recognition approaches (Carballido-Gamio *et al* 2004, Huang *et al* 2009). Jerebko *et al* (2007) combined ellipses fitted to individual horizontal cross-sections into final VB segmentations. Volumetric segmentation of VBs was presented in Davatzikos *et al* (2002) by registering a deformable shape model of the spine. Recently, Štern *et al* (2011) proposed a 3D segmentation technique for T2-weighted MR images which matched a parametric geometrical model of VBs derived from an elliptical cylinder. The method presented in this MR-based work extends segmentation of the VBs in 3D to provide higher precision and capture finer anatomical details of the VBs.

Both T1-weighted (T1w) and T2-weighted (T2w) MR imaging of the spine are used in clinical practice to assess the IVDs (Modic and Ross 2007). An IVD is composed of the central gel-like nucleus pulposus surrounded by the fibrous cartilage of the annulus fibrosus. In the T2w images, a healthy nucleus pulposus is imaged as a bright elliptical area generating high contrast signal in comparison with the hypo-intense region of the surrounding annulus fibrosus. In T2w images, the mean signal intensity value within the cancellous bone of the vertebrae is typically between the mean intensity values of the annulus fibrosus and the nucleus pulposus (examples in figure 1), allowing the use of edge detection techniques for IVD segmentation (Shi *et al* 2007). The generalized Hough transform is employed in the segmentation pipeline of Seifert *et al* (2009) where it is followed by region clustering using centres of gravity of the identified ellipse-like objects. Further landmarks are found by detecting disc edges by open active contours and used to drive active shape model (ASM) segmentation in the transverse plane. The 2D IVD contours are subsequently combined into a final 3D volume. Michopoulou

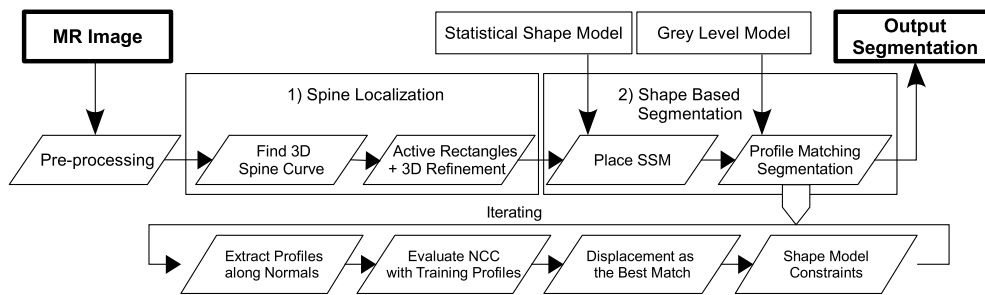


**Figure 2.** The segmentation procedure consists of two main steps. First, the spine is localized in the input image by automated spine curve extraction (1). Next, the SSMs are placed into initial positions along the defined spine curve and deformed to segment the new case (2).

*et al* (2009) present a semi-automatic segmentation of the IVDs from a T2w 2D sagittal slice by a combination of the fuzzy c-means and *a priori* knowledge from a probabilistic disc atlas, to deal with overlapping tissue classes. The method is further adapted to distinguish between healthy and degenerated IVDs.

Spine abnormalities can substantially complicate (semi)-automated segmentation approaches and specially adapted techniques are required in increasingly complex pathologies, such as scoliosis. Chevretil *et al* (2009) introduced a combination of edge detection techniques and texture analysis to perform an unsupervised 2D segmentation of IVDs from sagittal MR slices of scoliotic patients. All of the above mentioned techniques are based on 2D slice analysis, though Seifert *et al* (2009) have combined 2D segmentation results to provide a 3D volume. In contrast to these 2D approaches, our approach is intrinsically volumetric, utilizing the full multiplanar image information available from the current 3D MR imaging protocol for automated segmentation and classification of shape abnormalities of IVDs with degenerative changes.

## 2. Method

The segmentation strategy is based on the concept of ASMs, previously used in many medical imaging applications (Heimann and Meinzer 2009). Grey level models (GLMs) of intensity profiles extracted from the input MR images are used to drive the shape deformation.

The pipeline of the complete algorithm is illustrated in figure 2. The algorithm can be divided into two main parts: (1) spine localization and (2) shape-based segmentation of IVDs and VBs. During the spine localization, the 3D spine curve is extracted and approximate positions of VBs are determined by the use of active rectangles. The shapes are subsequently deformed using the ASM strategy.

In the remainder of this section, the image database and pre-processing steps are presented, followed by a description of the spine localization algorithm. Next, the method for generating the SSMs and GLMs is discussed before presenting the evaluation procedure to quantify the algorithm's performance.

### 2.1. Imaging database

MR images from 28 volunteer subjects (19 male, 9 female) were acquired from the lumbar (superiorly to VB L5) and lower-thoracic spine (inferiorly to VB T7 or T8) in two overlapping blocks using the T2w 3D SPACE pulse sequence on a Siemens 3T TRIO MR system. The

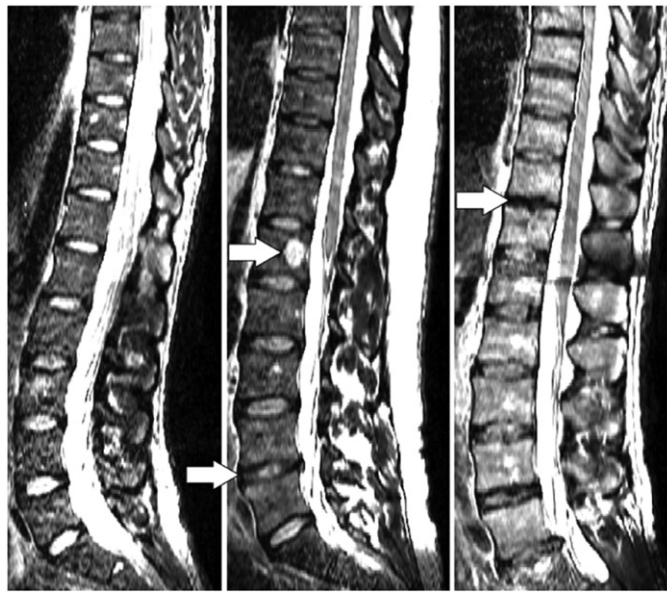


**Figure 3.** Example sagittal images from the image database. Although non-asymptomatic volunteers were scanned, a number of incidental radiological findings were observed in the sample. A bright haemangioma can be seen in the middle image in the area of vertebra L1 and early signs of degeneration at IVD L4/L5 (white arrows). The case on the right shows evidence of degenerative changes at IVD T11/T12 (white arrow). The image on the left exhibits imaging artifacts, perceptible as decreased SNR in the lumbar area.

acquisition time was 7 m 50 s per block. The SPACE sequence has shown good potential for clinical assessment and diagnostic purposes (Meindl *et al* 2009, Lighvani and Melhem 2009), and has the advantage of 3D volumetric acquisition providing high-resolution images with a good levels of anatomical detail (176 axial sections per block with  $0.34 \text{ mm} \times 0.34 \text{ mm}$  in-plane resolution and 1–1.2 mm slice thickness).

A subset of 14 cases (134 IVDs, 132 VBs) was manually segmented by AN (under expert supervision of CE) and used for quantitative evaluation of the automated algorithm as reported in the next section. The automated segmentation results for all 28 cases are reported online<sup>5</sup> for qualitative assessment.

All subjects were ‘asymptomatic’ healthy volunteers, self-reporting no major or chronic symptoms of back pain. The high prevalence of degenerative disc imaging finding in the asymptomatic population reported in clinical studies (Emch and Modic 2011) is in accordance with the findings observed in our database. Signs of degenerative changes were identified in 5 out of the 14 manually segmented cases (independently classified by CE and confirmed by expert radiologist DW) where 7 lumbar IVDs (1  $\times$  T12/L1, 1  $\times$  L1/L2, 1  $\times$  L2/L3, 1  $\times$  L3/L4, 3  $\times$  L4/L5) were marked as abnormal. These shapes were tested in the validation to assess the ability of the automated model to classify IVDs with degenerative signs based on 3D shape analyses. Incidental findings such as vertebral haemangiomas in three cases (visible as abnormally increased signal intensity as per example in figure 3) as well as Schmorl’s nodes in several cases (vertebral endplate fracture) of varying dimensions were observed in

<sup>5</sup> (Username: msk\_spine, Password: Review\_Neubert):  
([http://aehrc.com/msk\\_spine/Website\\_Spine/Space/webpages/Space\\_main.php](http://aehrc.com/msk_spine/Website_Spine/Space/webpages/Space_main.php)).



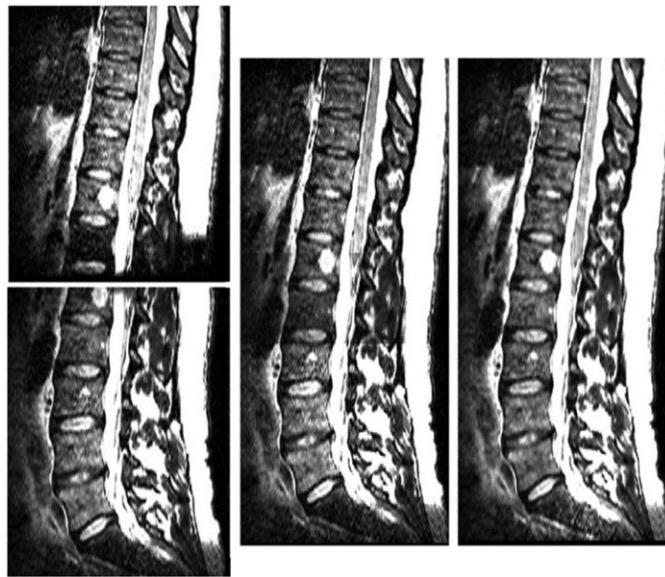


**Figure 4.** Intensity correction and block stitching. The original thoracic and lumbar slice blocks are shown separately (left) and following the stitching (middle). The applied pre-processing scheme reduces the signal intensity inhomogeneities at the block transitions and at the upper and lower vertical extremities of the merged image set (right).

the current MR dataset. A follow-up call was made with the subjects six months after the initial scans and two cases become symptomatic during this time (diagnosed with a central disc bulge and a posterior disc bulge). Both discs were marked in the original scans by the radiologist and consequently by the algorithm as abnormal.

The medical research ethics committee of the University of Queensland approved the current study and informed written consent was obtained from all participants involved.

## 2.2. Image pre-processing

In the present study, two (serial) blocks are merged together covering the lower thoracic and lumbar spine regions in one combined image set. A large overlap region between the two image blocks was used in acquisition to correct intensities at the upper and lower margins of the original image blocks with decreased signal-to-noise ratio (SNR) and contrast-to-noise ratio (CNR) characteristics (figure 4), and further enhancing steps were taken during the pre-processing.

First, a customized intensity adjustment based on the N4 bias field correction algorithm (Tustison and Gee 2009) is applied to the region of the spinal column to each block of images. The spine column (area of IVDs and VBs) is generated as a cylindrical region around the extracted spine curve (see next subsection Spine Localization), covering parts of IVDs and VBs without any external anatomy that could perturb the signal intensity adjustments (e.g. the bright spinal cord and surrounding cerebro-spinal fluid). Next, the individual image blocks are merged together based on the physical coordinate system of the lower (lumbar) image. The upper image is reformatted using B-Spline interpolation to fit the grid of the new coordinate system. Voxel intensities in the overlapping area are calculated as a weighted average between the two corresponding images to eliminate the strong intensity inhomogeneity

at the lower/upper part of the blocks. A second pass of the image intensity correction over the spinal column is applied, this time to the merged image, to further improve the smoothness of the merged image. Next, smoothing by anisotropic diffusion (15 iterations with the time step 0.01 and conductance 1.0) is applied to the corrected image to reduce acquisition noise and spurious discontinuities at the transitions. Finally, image histogram normalization is performed to standardize the intensity values by matching the histogram extracted from the spine column to a template one. An example image before and after correction is shown in figure 4.

### 2.3. Segmentation algorithm

The segmentation strategy is based on the method of the ASM originally introduced by Cootes *et al* (1995). An approximate localization of the spine and individual IVDs and VBs is needed to initialize the ASM. This subsection details the steps in the algorithm pipeline shown in figure 2 after pre-processing.

#### 2.3.1. Spine localization

First, the spine curve (a continuous line passing through the centres of IVDs and VBs in 3D) is extracted based on the algorithm proposed by Vrtovec *et al* (2007). This algorithm requires a seed point located within some of the imaged IVDs or VBs that is placed manually in Vrtovec *et al* (2007). To overcome the manual initialization, an automated procedure to find the seed point is proposed in this subsection together with an outline of the used algorithm (Vrtovec *et al* 2007). A new strategy (based on active rectangles) was implemented to determine the locations of IVDs and VBs and is presented in the second part of this subsection.

**2.3.1.1. Spine curve extraction.** A line of axial symmetry passing through the seed point is found for each axial cross-section by maximizing a similarity measure (the mutual information) and the IVD or VB centre is refined along this line by minimizing the operator  $\Gamma$  equation (1). The operator  $\Gamma$  proposed by Vrtovec *et al* (2007) defines  $M$  concentric rings of increasing radii and is computed as

$$\Gamma = \frac{\sum_{m=1}^M w_m H_m}{H \sum_{m=1}^M w_m}, w_m = e^{-\frac{1}{2} \left(\frac{m}{M} s\right)^2}, \quad (1)$$

where  $H_m = -\sum_{q=1}^Q p_{q,m} \log p_{q,m}$  is the entropy of image intensities under the  $m$ th ring defined by the probability distribution  $p_{q,m}$ ,  $Q$  is the number of histogram bins,  $H$  is the entropy of image intensities over the whole operator region (circle defined by the biggest ring) and  $s$  defines the standard deviation of the Gaussian weights  $w_m$ , favouring the smaller rings. The located centre of an IVD or a VB is also used as the initial point for the neighbouring slice and the search is expanded in both (superior and inferior) directions (a subset of axial slices distanced by 10 mm is used to save computational time). Subsequently, a robust 3D fitting of 3rd degree polynomials in each coordinate direction is performed using a nonlinear least trimmed squares regression method (Rousseeuw and Leroy 2003) to find the continuous spine curve in 3D (figure 5).

In this paper, we used the operator  $\Gamma$  to automatically find the initial seed point to initiate the spine curve extraction. An equidistant point grid  $\{g_i\}$  is defined (with spacing  $h_g$ ) in the middle axial slice where the operator is evaluated. Next, a neighbourhood average, weighted



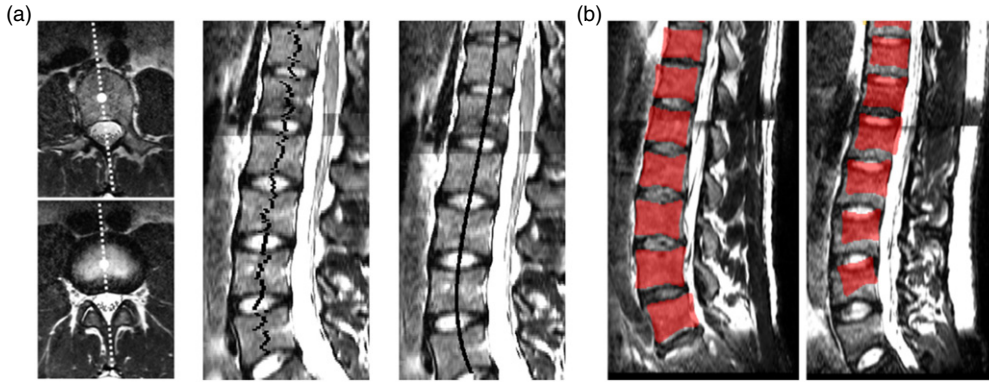


**Figure 5.** Extraction of the 3D spine curve and ASM initialization. Example axial slices with found lines of axial symmetry and centres of an IVD or a VB are shown (panel (a), left). The centres are projected into the middle sagittal image (panel (a), middle) and the fitted polynomial spine curve is shown (panel (a), right). Example initializations are shown for two cases in panel (b). The VB L5 is not detected in the case on the right due to the small field of view and intensity attenuation in the bottom of the image.

by the mean image intensity at grid points, is evaluated and the maximal point is taken as the seed point:

$$\hat{g}^{\text{seed}} = \arg \max_i \sum_{j \in N_i} \Gamma(g_j) I(g_j), \quad (2)$$

where  $N_i$  is a 4-connected neighbourhood of grid points centred at point  $g_i$  and  $I(\cdot)$  is the image intensity. The image term is added to favour the areas of a VB or nucleus pulposus against the darker muscular tissue that can also emerge in circular structures.

Numerical values of the parameters can be consulted in section 2.4. Most parameters can be empirically set to match the dimensions for VB or IVD detection. Anatomical studies show that the typical vertebral width (left–right) and length (inferior–superior) in the thoracic and lumbar area range between 20–50 mm and 15–35 mm, respectively (Masharawi *et al* 2008). The number of rings and their radii were chosen to cover an area with a diameter of 6 cm (30 rings with increasing radii of 1 mm) and no effects on  $\hat{g}^{\text{seed}}$  were observed when doubling the radii and reducing the number of discs to half (thus conserving the area). To further evaluate the sensitivity, we performed a small grid search for parameters  $Q$  (between 32, 64, 128) and  $s$  ( $\sqrt{2}$ ,  $\sqrt{10}$ ,  $\sqrt{20}$ ) on a subset of three subjects. No effects on  $\hat{g}^{\text{seed}}$  were observed by changing the values of  $s$ . In two cases, three different seed points were found for the three values of  $Q$ , but they all lied within the VB. In the remaining case, the same valid seed point inside a VB was found for  $Q = 32$  and  $Q = 64$  and an erroneous point lying slightly outside the VB was found for  $Q = 128$ .

**2.3.1.2. Active rectangles in the sagittal plane.** Locations of individual vertebrae are found using an active contour method in the form of interactive active rectangles, similarly to Abufadel *et al* (2006) but with a different cost function. A semi-affine transformation is applied to a unit square that is placed in the input MR image. The used cost function was proposed by McIntosh and Hamarneh (2012); equations (3), (4)) and includes four energy terms describing the matching of the following four quantities: the size of the rectangle, the edge strength along the rectangle contour, the mean and standard deviation of the image intensity inside the rectangle. Means and standard deviations of these measures were trained from the

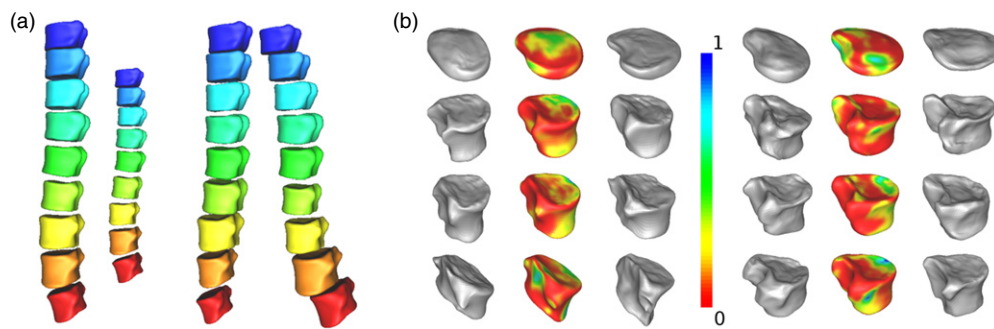


**Figure 6.** Model of the spine variability with the first two modes of variation (at  $\pm 2$  StDev) is shown in panel a). Mean shapes of the VBs are scaled and placed to the locations described by the model for visualization purposes. The first mode describes the elongation of the spine coupled with changes in the size of VBs, the second the extent of the lordosis. Statistical mean shapes of individual VBs and IVDs and their first mode of variation (shapes generated at  $\pm 3$  StDev) are shown in panel b). The lumbar IVDs (T12/L1-L4/L5) and L1, L3 and L5 VBs respectively are shown (left) and the thoracic IVD (T7/T8-T11/T12) and T8, T10, T12 vertebrae can be seen (right). The colour codes the relative variation of the first mode.

14 manually segmented images. In the interest of space, we refer the reader to McIntosh and Hamarneh (2012) for detailed description of the cost function and the four potentials.

A set of initial rectangles is placed along the spine curve at 10 mm intervals and optimized in the sagittal plane using the downhill simplex algorithm (Nelder and Mead 1965). The interval is small enough to allow the coverage of each VB by several rectangles. The optimized rectangles are combined to form a mask of vertebrae locations that is thresholded using an empirical threshold  $th = 4$  (i.e. four rectangles converged to the same location are required to detect a VB). The event of missing one single VB is automatically detected and corrected by taking the mean centre position and height of the neighbouring regions.

**2.3.1.3. Refinement of the rectangles in 3D.** With the active rectangles, initial locations of VB centres are obtained in the corresponding 2D slices. In this section, we describe how we use the cost function from McIntosh and Hamarneh (2012) to refine these positions in 3D and to correctly assign the VBs their labels (e.g. L5—fifth lumbar VB). For this purpose, a simplified model of the spinal shape in 3D is constructed. The simplified spine is described as a set of points identifying the centres of VBs (in 3D) and their heights, forming a set of four-dimensional points. The sets are aligned to the L1 VB and the principal component analysis is applied to identify the modes of variation (similarly to SSMs as described in section 2.3.2.1). Next, a simplified deformable spine model is constructed by placing the statistical mean shapes (from section 2.3.2.1) to the locations found by active rectangles (figure 6). This shape is optimized using the same cost function in 3D and the same algorithm (Nelder and Mead 1965) as for active rectangles. The result is refined to lie within 1.5 standard deviations of the modes of variations of the field model. In this manner, precise initialization for ASM can be obtained. Depending on the field of view, in some cases the active rectangles can miss the lower-most VB L5. By adding an additional VB below the lower-most position, a cost comparison of the optimized models can be done between the two configurations and the one with better fit is chosen as the final result.

The optimized simplified spine model serves as an initialization for the ASM of individual IVDs and VBs. The IVDs are placed to the middle of the ‘gap’ areas between the segmented VB regions.

### 2.3.2. Shape based segmentation.

**2.3.2.1. Statistical shape model and grey level model generation.** A SSM establishes and exploits point-wise correspondences among a dataset of training shapes  $\tilde{S}_i, i \in \{1, \dots, N\}$ , i.e. finds a mesh representation  $S_i$  of the training shape  $\tilde{S}_i$  that is as close to  $\tilde{S}_i$  as possible and has the same number of points for each shape in the dataset and these points are located at corresponding anatomical landmarks:

$$\tilde{S}_i = \{\tilde{x}_i^j \in \mathbb{R}^3 | j = 1, \dots, n_i\} \rightarrow S_i = \{x_i^j \in \mathbb{R}^3 | j = 1, \dots, n\}. \quad (3)$$

Supposing such a set  $S_i$  is available, the shapes can be aligned (the generalized Procrustes alignment (Gower 1975) is used in this work) and a point distribution can be defined for the positions of spatially corresponding shape vertices  $x_i^j \in \mathbb{R}^3$ . The mean positions  $\bar{x}$  and covariance matrix  $\mathbf{C}$  are computed<sup>6</sup>:

$$\bar{x} = \frac{1}{N} \sum_{i=1}^N x_i, \mathbf{C} = \frac{1}{N-1} \sum_{i=1}^N (x_i - \bar{x})(x_i - \bar{x})^T. \quad (4)$$

Each shape  $S_i$  is represented as an  $n$ -dimensional vector  $x_i$ . The shape vectors can be represented in the form of

$$x_i = \bar{x} + \mathbf{P}b_i = \bar{x} + \sum_{m=1}^N p^m b_i^m \quad (5)$$

where  $\mathbf{P} = \{p^m | m = 1, \dots, N\}$  are the eigenvectors of the covariance matrix  $\mathbf{C}$  (with corresponding eigenvalues  $\{\lambda^m | m = 1, \dots, N\}$ ) and  $b_i = \{b_i^m\}$  are the associated mode coefficients. By modifying the surface parameters  $b_i$ , new shapes similar to those in the training dataset can be generated (equation (5)). Only the  $M \leq N$  modes of variation corresponding to the largest eigenvalues are used because they describe most of the shape variation in the dataset.  $M$  is chosen such that the fraction of variance described:  $(\sum_{m=1}^M |\lambda^m| / \sum_{m=1}^N |\lambda^m|)$  is larger than a pre-set tolerance (see subsection 2.4).

The framework of finding point-wise correspondences of training shapes  $\tilde{S}_i$  is based on a groupwise optimization of the description length, an algorithm proposed by Davies *et al* (2002, 2008) (an in-house implementation of improved version from Davies *et al* (2008) was used in this work). First, the marching cubes algorithm (Lorensen and Cline 1987) is applied to each manually segmented binary volume  $B_i, i \in \{1, \dots, N\}$  to obtain mesh surfaces  $\tilde{S}_i$ , comprised of vertices  $\tilde{x}_i^j \in \mathbb{R}^3, j \in \{1, \dots, n_i\}$ . The anatomical shapes of IVDs and VBs are topologically equivalent to a genus 0 surface and therefore allow finding a bijective mapping to topologically simpler genus 0 surfaces, such as a sphere. In this study, the parameterizations were found using a spherical harmonic description SPHARM (Styner *et al* 2006). Consequently, a one-to-one sphere parameterization  $\varphi_i$  (Brechtbühler *et al* 1995) can be found and a sphere surface  $Sp_i$  is assigned to the shape  $S_i$ :  $Sp_i = \varphi_i(S_i)$ . The SSM is used to encode the shape information from the training database by projection onto the modes of variations of the SSM (equation (6)) and the shape is accordingly represented by the mode weights  $b_i^m$ :

$$b_i = \mathbf{P}^T(x_i - \bar{x}), \mathbf{P} = \{p^m | m = 1, \dots, M\} \quad (6)$$

The shape deformation procedure is driven by the GLM, consisting of extracted grey level intensity profiles centred at each vertex  $x_i^j$  and sampled along the vertex normal  $\vec{n}_i^j$  for all

<sup>6</sup> The following notations are used for reader's clarity. Subscript—iterates the shapes in the training database. Superscript—refers coordinates in a vector or matrix. Bold lower case—vectors. Bold upper case—matrices.  $x$  with a tilde superscript—refers to the original shape coordinates.  $x$  without the tilde superscript—refers to the optimized coordinates within the shape model.

**Table 1.** Algorithm parameters.

Symbol	Connotation	Value
$2L+1$	Points in training profiles	61
$h$	Profile spacing	0.25 (mm)
$M$	Number of co-centric rings (equation (1))	30
$Q$	Number of histogram bins (equation (1))	64
$s$	StDev of Gaussian weights (equation (1))	$\sqrt{10}$
$h_q$	Grid spacing (equation (2))	5 (mm)
$th$	Threshold for active rectangles	4
$2K+1$	Points in matching profiles (IVDs)	81
$2K+1$	Points in matching profiles (VBs)	161
$b_{\max}$	Shape constraint	2.0
$N_b$	Number of modes	Table 2
$N_{\text{iter}}$	Number of iterations	100

training shapes  $S_i$ ,  $i = 1, \dots, N$ . For each profile, the intensity values are extracted from the MR image using B-Spline interpolation of the intensities at equidistantly sampled points both inside and outside the shape. In this manner, each profile contains  $2L+1$  points ( $L$  inside,  $L$  outside plus one at the vertex) that are sampled along the normal with spacing  $h$  (the physical length of the profile being  $2L \cdot h$  mm). Consequently, each SSM vertex is assigned an array of  $N$  training profiles that will drive the segmentation.

**2.3.2.2. Shape deformation.** The shape deformation procedure providing the final segmentation results is an iterative process highlighted in figure 2, employing the above described SSM and GLM. Let us note the deforming shape  $V$  and its vertices  $v^j$ ,  $j = 1, \dots, n$ . At each iteration, grey level profiles  $\hat{p}^j$  of lengths  $2K+1 > 2L+1$  (length of the training profiles) are extracted (with the same spacing  $h$ ) for each vertex  $v^j$  of the positioned shape. The computation of the optimal displacement  $\mathbf{d}^j$  of each vertex starts by extracting sub-profiles  $\hat{p}^{j,k}$ ,  $k = 1, \dots, 1+K-L$  of length  $2L+1$  from  $\hat{p}^j$  by moving the profile centre point. These profiles are normalized to zero mean and unit variance and compared to all training profiles  $p_i^j$ ,  $i = 1, \dots, N$  (also normalized) of the corresponding vertex  $v^j$  by evaluating the normalized cross-correlation metric (NCC) (equation (7)) and the profile  $\hat{p}^{j,k_{\max}}$  maximizing the similarity metric is determined:

$$\hat{p}^{j,k_{\max}} \leftarrow \arg \max_{i,k} \text{NCC}(\hat{p}^{j,k}, p_i^j), \text{NCC}(a, b) = \frac{a \cdot b}{\|a\| \|b\|}. \quad (7)$$

The centre  $v^{j,k_{\max}}$  of this profile  $\hat{p}^{j,k_{\max}}$  determines the optimal displacements of the corresponding vertex  $v^j$  as  $\mathbf{d}^j = v^{j,k_{\max}} - v^j$ . Subsequently, the overall shape displacement is restrained by the modes of variation of the SSM to preserve the anatomical validity of the shape.

#### 2.4. Algorithm setup and parameters

Numerical values of used parameters can be consulted in table 1. The obtained SSMs were used to constrain the shape deformation during the segmentation procedure with the shape constraint  $b_{\max} = 2.0$  StDev, and the number of modes  $N_b$  was determined to explain 90% of the total variation within the SSM (table 2).

**Table 2.** Modes of variation of the statistical shape models (L—lumbar, T—thoracic).

SSM	#Shapes	Modes to explain 90% variation
IVD-L (T12/L1-L4/L5)	69	8
IVD-T (T7/T8-T11/T12)	65	9
VB-T8	11	6
VB-T9	14	7
VB-T10	13	6
VB-T11	13	5
VB-T12	13	6
VB-L1	14	6
VB-L2	13	5
VB-L3	13	5
VB-L4	14	5
VB-L5	14	5

### 2.5. Validation

The automated segmentation algorithm was applied to the entire set of scans from 28 subjects and the qualitative results can be accessed online (section 2.1). Quantitative measures reported here were evaluated from the results on the subset of 14 scans with the available ground truth. These images were segmented using a leave-one-out strategy (each currently segmented shape was omitted from the SSM and GLM). To compare the automatic segmentation results (binary image  $A$ ) against the manually contoured ground truth (binary image  $M$ ), the Dice similarity coefficient (DSC) value (equation (8)), the mean absolute shape distance (MASD) and Hausdorff distance were computed:

$$\text{DSC}(A, M) = 2 \frac{|A \cap M|}{|A| + |M|}. \quad (8)$$

To obtain the MASD and Hausdorff distance, for each point  $i$  in  $A$  the minimum distance  $d_i^{AM}$  to all points in  $M$  is determined. The average directed surface distance ( $\text{ASD}_{AM} = \text{average}\{d_i^{AM}\}$ ) and directed Hausdorff distance ( $H_{AM} = \max\{d_i^{AM}\}$ ) is calculated. The same calculation is performed for each point in  $M$  to all points in  $A$ , with the mean average surface distance ( $\text{MASD} = (\text{ASD}_{AM} + \text{ASD}_{MA})/2$ ) and Hausdorff distance ( $\text{HD} = \max(H_{AM}, H_{MA})$ ) then calculated. The distance between surfaces was calculated in voxel space using the signed exact Euclidean distance transform (Maurer and Raghavan 2003).

## 3. Results

### 3.1. Initialization

The VB detection was successful in locating 257 of the 261 VBs (98.5%) from 28 subjects. In four cases the lower-most L5 VB was not detected. In this scenario, a simple input to the algorithm is required to add an additional VB below the lower-most detected one. Accuracy of the initialization step (mean DSC) is reported with the segmentation results in table 3 (column Init DSC).

### 3.2. Statistical shape models

Four SSMs were built initially, one for lumbar and thoracic IVDs and VBs. Anatomical differences among the VBs are reflected by the SSMs (figure 7) where a distinct cluster

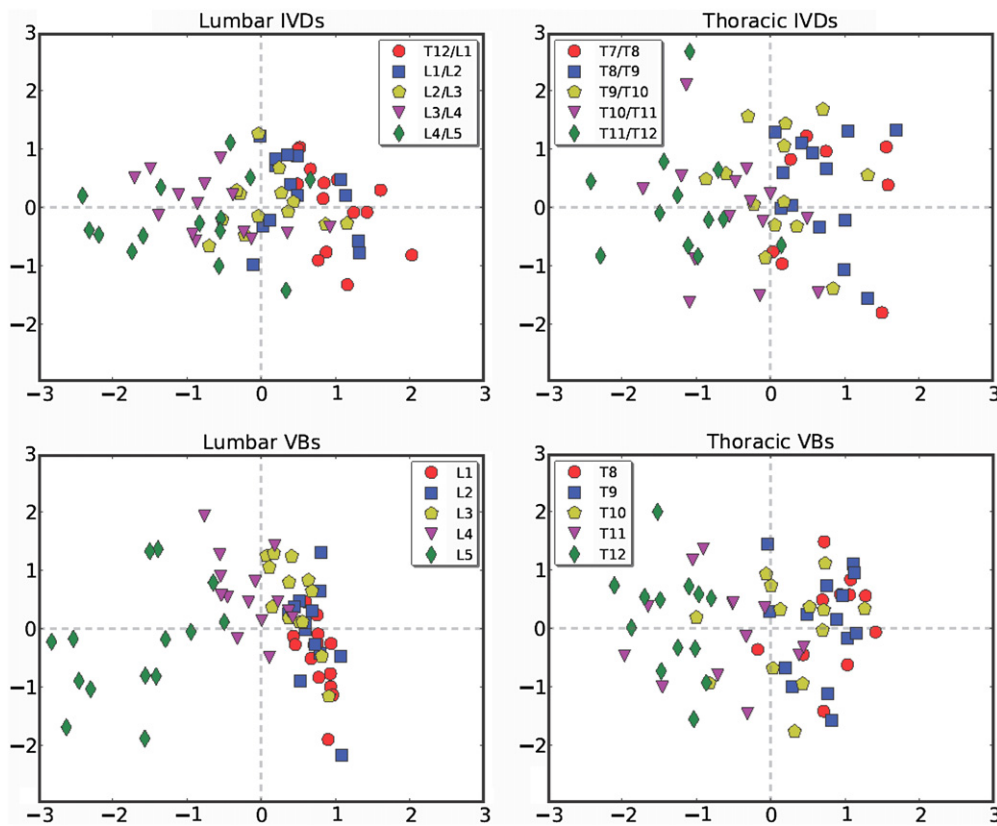


**Figure 7.** Eigenplots for the SSM of lumbar (left) and thoracic (right) IVDs (upper panel) and VBs (lower panel). This diagram plots the projection equation (6) of each shape onto the first (horizontal axis) and second (vertical axis) most important mode of variation. For the lumbar VBs, the large interclass shape differences are observed for the L5 and, in part the L4, VBs in keeping with the anatomical features of these caudal vertebrae. For the lower thoracic VBs, the larger interclass shape differences are observed for the T12 and T11 VBs. Interclass shape differences are less obvious for the lumbar and thoracic IVDs based solely on the first two modes.

**Table 3.** Quantitative segmentation results (L—lumbar, T—thoracic, H.Dist.—Hausdorff distance). The lumbar IVDs marked as degenerative are reported separately (row ‘L-IVD Deg’). The mean DSC for the initially placed mean shapes are reported for comparison (column ‘Init DSC’).

Anatomy	Count	Init DSC	DSC	DSC	DSC	MASD	MASD	MASD	H.Dist.	H.Dist.	H.Dist
		Mean	Mean	Min	StDev	Mean	Max	StDev	Mean	Max	StDev
L-IVD	68	0.690	0.893	0.803	0.031	0.594	1.112	0.176	3.869	7.200	1.251
T-IVD	46	0.764	0.883	0.826	0.024	0.483	0.739	0.098	3.069	7.956	1.007
L-VB	67	0.717	0.914	0.840	0.020	0.680	1.513	0.200	4.149	7.434	0.950
T-VB	59	0.642	0.901	0.860	0.016	0.659	1.041	0.128	4.003	6.949	0.928
L-IVD Deg	7	0.484	0.890	0.873	0.013	0.706	1.020	0.218	3.944	6.149	1.427

of mutually similar VBs can be identified—e.g. T11-T12 compared to T8-T10, and more noticeably L5 against other lumbar VBs. Due to the large differences in anatomical shape of the VBs, 10 SSMs specific to each VB (from T8 to L5) were generated and used to better model shape variations distinctive to each VB. For the IVDs, the two initial SSMs of lumbar



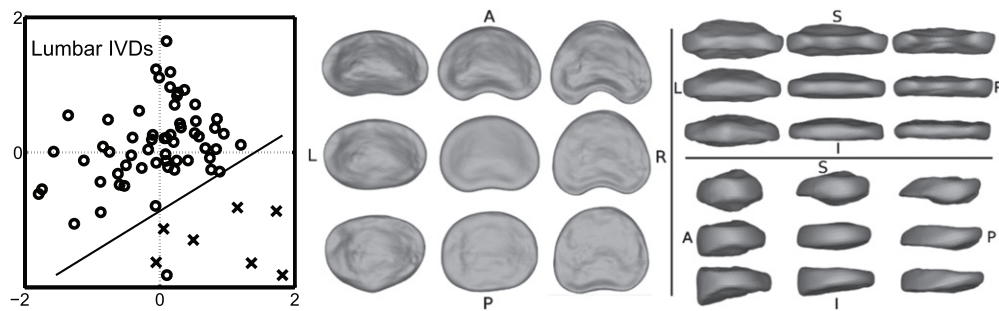


**Figure 8.** Automatically segmented shapes of lumbar IVDs are projected to the first (horizontal axis) and second (vertical axis) modes of variation of the SSM. Healthy IVDs are marked with a circle, IVDs with degenerative changes with a cross. The line delimiter in the graph represents the boundary of an automated classifier based on linear discriminant analysis that achieves a sensitivity of 100% and specificity of 98.3%. Corresponding shapes generated at  $\pm 3$  StDev of the first and second mode of variation are presented: views from the top (middle column), front (top right) and side (bottom right)—the mean shape in the centre, first mode horizontally, second mode vertically (orientations: A—anterior, P—posterior, L—left, R—right, S—superior, I—inferior).

(T12/L1 – L4/L5) and thoracic IVDs (T7/T8–T11/T12) were used as the IVDs generally exhibited less specific differences in shape across the spinal column (reflected by the SSM in figure 6). All SSMs were comprised of 4098 vertices. The mean shapes and primary modes of variation for the SSMs are illustrated in figures 6 and 8.

The SSM presented in figure 8 shows the anatomical variation of lumbar IVDs in more details. The first (horizontal axis) and second (vertical axis) mode of variation capture together the changes from circular-like discs (L3/L4, L4/L5) towards ‘bean’ shaped discs (T12/L1, L1/L2). The first mode also captures the changing inferior–superior thickness of the disc. The second mode describes the variation of the disc thickness and wedging in the anterior–posterior direction. The properties of the SSM of lumbar IVDs are discussed below in order to determine a possible use in the context of disc degeneration and automated classification.

### 3.3. Segmentation accuracy

Summary data for the comparisons between the manual and automated segmentation measurements are reported in table 3 and presented in histogram format in figure 9. Example segmentation results are shown at figure 10. Inaccuracy can be observed in some thoracic VBs (white arrows in figure 10), however most of the VBs, including those with haemangioma or with adjacent degenerate IVDs, are segmented with good accuracy. Similarly, most of the IVDs are segmented with satisfactory accuracy, including those with decreased signal intensity representative of degenerative change (L4/L5 IVD of the middle image and T11/T12 IVD of the right image).

### 3.4. Disc classification

The generated SSM of lumbar IVDs was studied to automatically detect IVD degenerative changes presenting as asymptomatic (early sub-clinical) disc degeneration. Plots of the first two shape parameters **b** (equation (6)) of the automatically segmented IVDs are shown in figure 8.

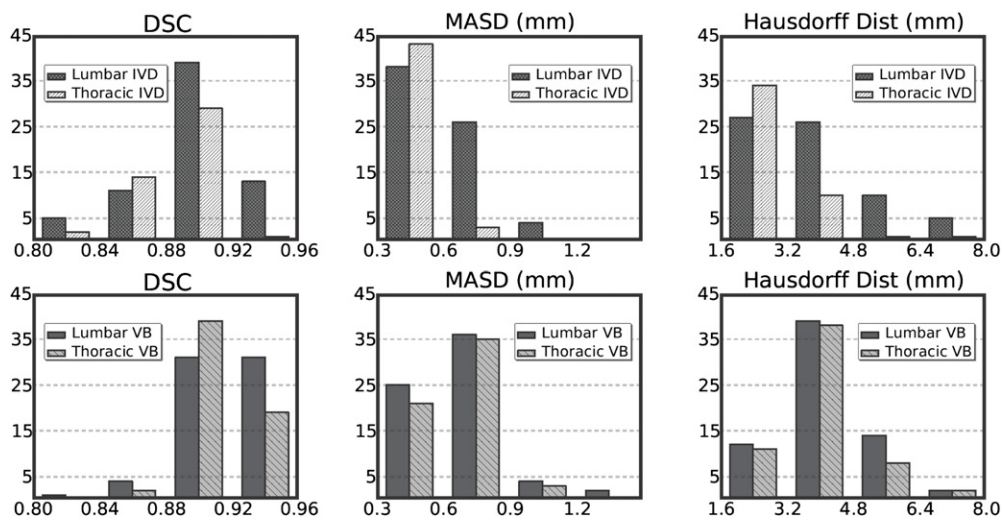


**Figure 9.** Histogram of DSC values, MASD (mm) and Hausdorff distances (mm) for the automated segmentation results of IVDs and VBs.

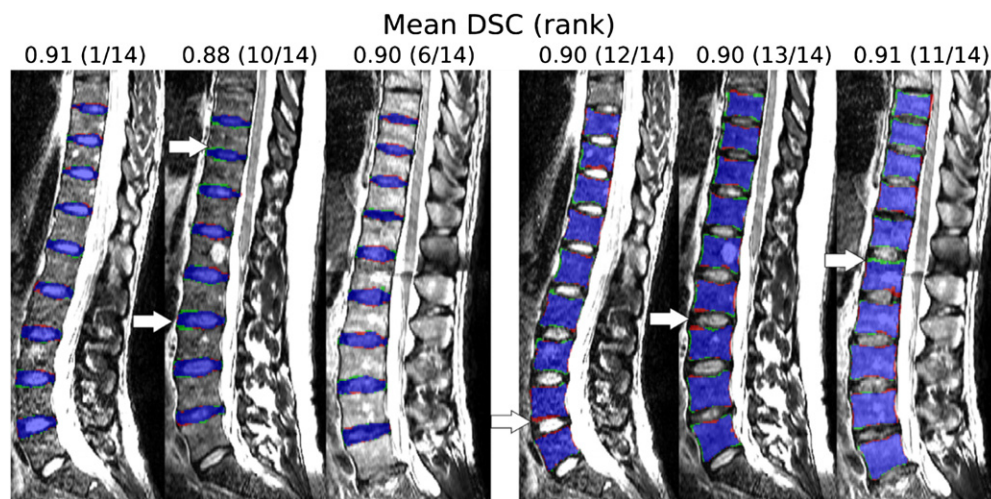


**Figure 10.** The same three slices from figure 3 are shown with overlaid segmentation results. The ground truth manual segmentations are shown in green, the automated segmentation results in red and the overlap in blue. Good results can be observed for most IVDs, including the L4/L5 (middle column, lower-most) and T11/T12 (right column, 4th from the top) disc with mild degenerative changes. Similarly, high precision has been achieved for most VBs, including the case with a vertebral haemangioma (middle image). Some inaccuracies are marked with white arrows.

The image database contains 7 lumbar IVDs with early disc degeneration. In figure 8, these cases are marked with a cross. A linear discriminant analysis classifier separated the two groups based on the first two shape parameters that describe the two most important modes of variation. A good descriptive power of the classifier can be noted with the sensitivity of 100% and specificity of 98.3%. The discs with degenerative changes appear in the bottom right area

of the plot (which could be used for automatic signalling of these discs for further assessment) indicative of a relative disc thinning (figure 8).

### 3.5. Computational time

The calculations were performed as a single thread on an Intel 2.83 GHz Dual Core PC with 8 GB RAM. An average time per iteration to segment an IVD is 26 s and 21 s for a VB. Several computational optimization strategies can be implemented to reduce the time, such as parallelization of the profile matching.

## 4. Discussion

### 4.1. Imaging database

In the present MR-based study, the SPACE sequence provided high resolution 3D images from which our innovative automated segmentation algorithm extracted detailed 3D shape information about IVDs and VBs. The SPACE sequence combining high spatial resolution, reduction in blurring and good sensitivity to spine pathologies demonstrated its effectiveness in evaluating degenerative disc disease (Lighvani and Melhem 2009). Some limitations against wide use in clinical practice arise from idiosyncratic artefacts (lower CNR, variable inter-subject SNR) that can however be addressed with advanced post-processing techniques, as presented here. In addition, compared to single 2D high resolution images (e.g. 0.3 mm  $\times$  0.3 mm) currently acquired in clinical practice, the anatomical edges appear less distinct in the SPACE images which necessitates advanced segmentation techniques. Nevertheless, the sequence provides excellent high resolution 3D information about IVD and VB shapes, not available previously. The 3D shape information accurately extracted by an automated segmentation algorithm provides the opportunity to examine early signs of disc degeneration in a new way.

### 4.2. Segmentation accuracy

Comparisons among 2D and 3D segmentation techniques validated on databases with varying image dimensions are difficult since the available information, the outputs (and complexity) differ substantially. The MR dataset used in this study is novel in its own right and the main drivers of this work are the challenges for automated 3D segmentations arising from its nature (high resolution, varying SNR, lower CNR).

An overview of quantitative results from the literature is given in table 4. Automatic segmentation of VB volumes in 3D from MR images has been achieved with a mean DSC of  $0.815 \pm 0.036$  (including the spinal cord) by Davatzikos *et al* (2002) or mean distance between manually annotated anatomical landmarks and automatically obtained segmentations of  $1.85 \pm 0.47$  mm by Štern *et al* (2011). A semi-automatic approach of Hoad and Martel (2002) achieved an accuracy of  $1.11 \pm 0.16$  mm for VBs. Our method quantitatively outperformed the above approaches, however (as stated previously), a direct comparison is not straightforward. The higher mean distances in the referenced studies can be partially attributed to using images with a higher inter-slice gap (around 3 mm). Our low MASD of  $0.67 \pm 0.17$  mm for the VBs is attributable to both the accuracy of the algorithm and the high resolution MR image dataset. The best approaches to segmenting the vertebrae (including the morphologically complex pedicles and processes) in 3D from CT images achieve a mean vertex-to-surface error  $0.95 \pm 0.91$  mm (Ma *et al* 2010). Nevertheless, the favourable comparisons demonstrate the applicability of the proposed method.

**Table 4.** Comparative results from literature (V—whole vertebrae, surf.—surface, dist.—distance).

Authors	Anatomy	Modality	Measure	Mean values
Davatzikos <i>et al</i> (2002)	VB-3D	MR	DSC	0.815
Štern <i>et al</i> (2011)	VB-3D	MR	Landmark dist.	1.85 mm
Hoad and Martel (2002)	V-3D	MR		1.11 mm
Klinder <i>et al</i> (2009)	V-3D	CT	Point-surf. dist.	1.12 mm
Ma <i>et al</i> (2010)	V-3D	CT	Point-surf. dist.	0.95 mm
Chevrefils <i>et al</i> (2009)	IVD-2D	MR	DSC	0.85
Michopoulou <i>et al</i> (2009)	IVD-2D	MR	DSC	0.92
			MASD	0.61 mm
Seifert <i>et al</i> (2009)	IVD-2D/3D	MR	DSC	0.84–0.98
			MASD	1.86–2.5 mm
			Hausdorff dist.	3.12–6.62 mm
Current study	IVD-3D	MR	DSC	0.89
			MASD	0.55 mm
			Hausdorff dist.	3.55 mm
Current study	VB-3D	MR	DSC	0.91
			MASD	0.67 mm
			Hausdorff dist.	4.08 mm

To our knowledge, the IVDs have been previously segmented using only 2D techniques. Michopoulou *et al* (2009) reported with their semi-automatic approach a mean DSC of 0.92 and mean MASD 0.98 pixels (translating to 0.613 mm) for normal IVDs in a 2D slice. Seifert *et al* (2009) combined a set of 2D IVD segmentations into 3D volumes of cervical and upper thoracic IVDs, achieving mean DSC values (excluding the challenging C2/C3 IVD) between 0.84 and 0.98 (for each disc level), mean MASD values between 1.19 and 1.61 pixels (translating to 1.86–2.5 mm) and mean Hausdorff distance between 2.00 and 4.24 pixels (3.12–6.62 mm). Our mean DSC values of 0.89 and 0.88 (lumbar and thoracic IVDs respectively) are at the lower end of these reported numbers, due to the 3D nature of our data and stronger imaging artefacts. The MASD metric compares favourably for our approach but the different image resolutions ( $1.562 \times 1.562 \times 1.16 \text{ mm}^3$  in Seifert *et al* 2009) make it difficult to score one method over another. In summary, the results appear favourable to those published in literature while noting that our MR data represent the most advanced level of spine imaging with fine detail that, to the best of our knowledge, have not been automatically segmented before.

#### 4.3. Disc classification

The shape parameters describing the extracted 3D volumes of lumbar IVDs allowed successful identification (100% sensitivity, 98.3% specificity) of IVDs with early degenerative changes in the asymptomatic subjects examined in this research. One misclassified healthy disc was found by the linear discriminant analysis in figure 8, which although thinner had a well defined nucleus pulposus with non-attenuated signal. This suggests that further characteristics are probably needed for more robust classification (e.g. anatomical measures, such as disc volumes, heights, widths or average/local thickness—all available with the proposed algorithm, or the signal intensity values inside the nucleus pulposus). Indeed, disc degeneration is a complex pathological process affecting the disc shape and internal structure with clinical diagnoses typically undertaken using a combination of morphological and signal (biochemical) features. At this stage no definite conclusions can be drawn from this small sample, however these promising preliminary results, currently based on disc shape descriptors alone, are supportive

and indicative of the potential of SSMs for automatic detection and classification of disc abnormalities.

#### 4.4. Study limitations and future work

Although the segmentation and disc classification results are very promising, there are some limitations that should be acknowledged and will be addressed in future work. Namely, the current study was performed on a dataset of asymptomatic subjects. These cases however exhibited signs of early disc degeneration in 36% cases, and several vertebral haemangioma and Schmorl's nodes were also observed. Since clinical studies indicate that the relationship between radiological findings of disc degeneration and patient symptoms is still unclear (Modic and Ross 2007), it can be argued that the presence of abnormalities (although asymptomatic) is adequate to validate the segmentation approach, particularly if the focus is on detection of early changes. Nonetheless, we are currently proceeding with an investigation into the use of the algorithm on a larger dataset of T2w scans from routine (2D) clinical images. The database will include symptomatic pathological subjects exhibiting degenerative changes of varying severity. The high resolution shape models should include necessary *a priori* information for successful segmentation on clinical images with a higher inter-slice gap.

### 5. Conclusion

High resolution 3D spine scans have the potential to deliver pre-programmed analysis of anatomical metrics, such as disc volumes or thickness. These metrics can provide advanced surrogate measures for use in clinical research studies concerned with quantifying early degenerative changes, but necessitate automated segmentation approaches to extract them. A new method for the 3D segmentation of VBs and IVDs from the thoracolumbar region has been presented in this work and validated on a dataset of high resolution 3D MR SPACE scans. The presented method has provided accurate 3D delineations of IVDs and VBs. Results of the experiments on spine images from a cohort of asymptomatic individuals compare favourably to other 3D MR segmentation techniques for VBs. It is the first time that an intrinsically 3D approach has been presented for segmentation of IVDs from volumetric scans.

Furthermore, the results suggest that the shape descriptors obtained from constructed models may provide important information about the changes in disc structure/morphology associated with early stages of degenerative processes. Such methods have the potential to supply an objective method for clinical trials and investigations for prospective evaluation of progressive disc degeneration.

### Acknowledgments

The authors would like to thank Dr Duncan Walker, radiologist at The Wesley Hospital, Brisbane, Australia, for his help with intervertebral disc assessment and classification. This research was supported under Australian Research Council's Linkage Projects funding scheme LP100200422.

### References

- Abufadel A, Slabaugh G, Unal G, Zhang L and Odry B 2006 Interacting active rectangles for estimation of intervertebral disk orientation *ICPR'06: Proc. 18th Int. Conf. on Pattern Recognition* (Hong Kong: IEEE) pp 1013–6



- Auerbach J D, Johannessen W, Borthakur A, Wheaton A J, Dolinskas C A, Balderston R A, Reddy R and Elliott D M 2006 *In vivo* quantification of human lumbar disc degeneration using T(1rho)-weighted magnetic resonance imaging *Eur. Spine J.* Suppl 3 **15** S338–44
- Ballard D H 1981 Generalizing the Hough transform to detect arbitrary shapes *Pattern Recognit.* **13** 111–22
- Berger R, Fenty M, Fry B, Maurer P M, Elliott D M and Borthakur A 2011 Improving predictability of painful discs by using T1ρ MRI and disc height *Proc. Int. Society for Magnetic Resonance in Medicine (ISMRM) Scientific Meeting* vol 31 p 420
- Brechtbühler C, Gerig G and Kübler O 1995 Parametrization of closed surfaces for 3D shape description *Comput. Vis. Image Understand.* **61** 154–70
- Carballido-Gamio J, Belongie S J and Majumdar S 2004 Normalized cuts in 3-D for spinal MRI segmentation *IEEE Trans. Med. Imaging* **23** 36–44
- Chevreteffs C, Chérier F, Aubin C-E and Grimard G 2009 Texture analysis for automatic segmentation of intervertebral disks of scoliotic spines from MR images *IEEE Trans. Inf. Technol. Biomed.* **13** 608–20
- Cootes T F *et al* 1995 Active shape models-their training and application *Comput. Vis. Image Understand.* **61** 38–59
- Cousins J P and Haughton V M 2009 Magnetic resonance imaging of the spine *J. Am. Acad. Orthop. Surg.* **17** 22–30
- Davatzikos C, Liu D, Shen D and Herskovits E H 2002 Spatial normalization of spine MR images for statistical correlation of lesions with clinical symptoms *Radiology* **224** 919–26
- Davies R H, Twining C J, Cootes T F, Waterton J and Taylor C 2002 3D statistical shape models using direct optimisation of description length *ECCV 2002: Eur. Conf. on Computer Vision* (Berlin: Springer) vol 2352 pp 1–17
- Davies R H, Twining C J and Taylor C 2008 Groupwise surface correspondence by optimization: representation and regularization *Med. Image Anal.* **12** 787–96
- Emch T M and Modic M T 2011 Imaging of lumbar degenerative disk disease: history and current state *Skeletal Radiol.* **40** 1175–89
- Fries P, Runge V M, Kirchin M A, Watkins D M, Buecker A and Schneider G 2008 Magnetic resonance imaging of the spine at 3 Tesla *Semin. Musculoskeletal Radiol.* **12** 238–52
- Gower J C 1975 Generalized procrustes analysis *Psychometrika* **40** 33–51
- Heimann T and Meinzer H-P 2009 Statistical shape models for 3D medical image segmentation: a review *Med. Image Anal.* **13** 543–63
- Hoad C L and Martel A L 2002 Segmentation of MR images for computer-assisted surgery of the lumbar spine *Phys. Med. Biol.* **47** 3503–17
- Huang S-H, Chu Y-H, Lai S-H and Novak C L 2009 Learning-based vertebra detection and iterative normalized-cut segmentation for spinal MRI *IEEE Trans. Med. Imaging* **28** 1595–605
- Jerebko A K, Schmidt G P, Zhou X, Bi J, Anand V, Liu J, Schoenberg S O, Schmucking I, Kiefer B and Krishnan A 2007 Robust parametric modeling approach based on domain knowledge for computer aided detection of vertebrae column metastases in MRI *IPMI'07: Proc. 20th Int. Conf. on Information Processing in Medical Imaging* (Berlin: Springer) pp 713–24
- Kim Y and Kim D 2009 A fully automatic vertebra segmentation method using 3D deformable fences *Comput. Med. Imaging Graph.* **33** 343–52
- Klinder T, Ostermann J, Ehm M, Franz A, Kneser R and Lorenz C 2009 Automated model-based vertebra detection, identification and segmentation in CT images *Med. Image Anal.* **13** 471–82
- Lichy M P *et al* 2005 Magnetic resonance imaging of the body trunk using a single-slab, 3-dimensional, T2-weighted turbo-spin-echo sequence with high sampling efficiency (SPACE) for high spatial resolution imaging: initial clinical experiences *Invest. Radiol.* **40** 754–60
- Lighvani A A and Melhem E R 2009 Advances in high-field MR imaging of the spine *Appl. Radiol.* **38** 18–27
- Lorensen W E and Cline H E 1987 Marching cubes: a high resolution 3D surface construction algorithm *Comput. Graph.* **21** 163–9
- Ma J, Le L, Zhan Y, Zhou X, Salganicoff M and Krishnan A 2010 Hierarchical segmentation and identification of thoracic vertebra using learning-based edge detection and coarse-to-fine deformable model *Proc. Int. Conf. on Medical Image Computing and Computer Assisted Intervention* pp 19–27
- Masharawi Y, Salame K, Mirovsky Y, Peleg S, Dar G, Steinberg N and Herskovitz I 2008 Vertebral body shape variation in the thoracic and lumbar spine: characterization of its asymmetry and wedging *Clin. Anat.* **21** 46–54
- Maurer C R and Raghavan V 2003 A linear time algorithm for computing exact Euclidean distance transforms of binary images in arbitrary dimensions *IEEE Trans. Pattern Anal. Mach. Intell.* **25** 265–70
- McIntosh C and Hamarneh G 2012 Medial-based deformable models in nonconvex shape-spaces for medical image segmentation *IEEE Trans. Med. Imaging* **31** 33–50



- Meindl T, Wirth S, Weckbach S, Dietrich O, Reiser M and Schoenberg S O 2009 Magnetic resonance imaging of the cervical spine: comparison of 2D T2-weighted turbo spin echo, 2D T2\*-weighted gradient-recalled echo and 3D T2-weighted variable flip-angle turbo spin echo sequences *Eur. Radiol.* **19** 713–21
- Michopoulou S K, Costaridou L, Panagiotopoulos E, Speller R, Panayiotakis G and Todd-Pokropek A 2009 Atlas-based segmentation of degenerated lumbar intervertebral discs from MR images of the spine *IEEE Trans. Biomed. Eng.* **56** 2225–31
- Modic M T and Ross J S 2007 Lumbar degenerative disk disease *Radiology* **245** 43–61
- Nelder J A and Mead R 1965 A simplex method for function minimization *Comput. J.* **7** 308–13
- Rousseeuw P J and Leroy A M 2003 *Robust Regression and Outlier Detection (Wiley Series in Probability and Statistics)* (New York: Wiley-Interscience)
- Seifert S, Wachter I, Schmelzle G and Dillmann R 2009 A knowledge-based approach to soft tissue reconstruction of the cervical spine *IEEE Trans. Med. Imaging* **28** 494–507
- Shi R, Sun D, Qiu Z and Weiss K L 2007 An efficient method for segmentation of MRI spine images *Proc. IEEE Int. Conf. on Complex Medical Engineering* pp 713–7
- Štern D, Likar B, Pernuš F and Vrtovec T 2011 Parametric modelling and segmentation of vertebral bodies in 3D CT and MR spine images *Phys. Med. Biol.* **56** 7505–22
- Styner M, Oguz I, Xu S, Brechbühler C, Pantazis D and Gerig G 2006 Statistical shape analysis of brain structures using SPHARM-PDM *Insight J.* (Special edition on MICCAI Open Science Workshop) **1071** 242–50
- Tustison N J and Gee J C 2009 N4ITK: Nick's N3 ITK implementation for MRI bias field correction *Insight J.* **2009** 1–8
- Vrtovec T, Ourselin S, Gomes L, Likar B and Pernuš F 2007 Automated generation of curved planar reformations from MR images of the spine *Phys. Med. Biol.* **52** 2865–78
- Woolf A D and Pfleger B 2003 Burden of major musculoskeletal conditions *Bull. World Health Organ.* **81** 646–56
- Yu H J, Bahri S, Muftuler L T, Nalciaglu O and Gardner V 2011 Correlation between ADC and T1 $\rho$ -Relaxation time for *in-vivo* assessment of intervertebral disc degeneration *Proc. Int. Soc. for Magnetic Resonance in Medicine (ISMRM) Scientific Meeting* vol 19 p 3242